

Cite this article as: Li Yanping, Huang Wei, He Yan, et al. Early Crack Propagation Behavior of Laser Metal Deposited Ti-6Al-4V Alloy Under High Cycles Fatigue Loading[J]. Rare Metal Materials and Engineering, 2025, 54(01): 62-75. DOI: 10.12442/j.issn.1002-185X.20240580.

ARTICLE

# Early Crack Propagation Behavior of Laser Metal Deposited Ti-6Al-4V Alloy Under High Cycles Fatigue Loading

Li Yanping<sup>1</sup>, Huang Wei<sup>1</sup>, He Yan<sup>1</sup>, Xu Feng<sup>2</sup>, Zhao Sihan<sup>1</sup>, Guo Weiguo<sup>1</sup>

<sup>1</sup>School of Aeronautics, Northwestern Polytechnical University, Xi'an 710072, China; <sup>2</sup>School of Astronautics, Northwestern Polytechnical University, Xi'an 710072, China

**Abstract:** The crack initiation and early propagation are of great significance to the overall fatigue life of material. In order to investigate the anisotropic fracture behavior of laser metal deposited Ti-6Al-4V alloy (LMD Ti64) during the early stage, the four-point bending fatigue test was carried out on specimens of three different directions, as well as the forged specimens. The results indicate the anisotropic crack initiation and early propagation of LMD Ti64. The direction perpendicular to the deposition direction exhibits a better fatigue resistance than the other two. The crack initiation position and propagation path are dominated by the microstructure in the vicinity of U-notch. LMD Ti64 has a typical small crack effect, and the early crack propagation velocities in three directions are similar. Affected by the slip system of LMD Ti64, secondary cracks frequently occur, which are often found to have an angle of 60° to the main crack. The electron backscatter diffraction analysis indicates that LMD Ti64 has preferred orientations, i. e., strong  $\langle 0001 \rangle // Z$  texture and  $\langle 001 \rangle // Z$  texture. Their crystallographic orientation will change as the direction of columnar  $\beta$  grains turns over, resulting in the fatigue anisotropy of LMD Ti64 in crack initiation and early crack propagation process.

**Key words:** fatigue resistance; crack propagation behavior; microstructure; laser metal deposit; Ti-6Al-4V; anisotropy

Over the past decade, additive manufactured (AM) titanium alloys have met a noteworthy increase in biomedicine and aerospace owing to their extraordinary performances in strength, fracture toughness, corrosion resistance and cryogenic mechanical properties. In particular, Ti-6Al-4V (Ti64) has become the most pervasive commercial AM titanium alloy in service. As a versatile option for manufacturing or repairing AM components, laser metal deposition (LMD) technique combines laser and powder processing and enhance material utilization by enabling manufacture of high precision near net shape components from powders, which has attracted great research interest<sup>[1]</sup>. For AM components inevitably suffering from complex cyclic loadings, high cycle fatigue ( $10^5 - 10^7$  cycles) is the most important cause of failure<sup>[2]</sup>. Various factors affecting material fatigue resistance can be divided into internal causes (residual stress, surface quality, defects, microstructure, etc) and external causes (loading mode, stress ratio, frequency, etc), so they have become a hot topic for the researchers. Only the

internal causes herein were analyzed.

Residual stress will significantly reduce the fatigue resistance of AM Ti64, and stress release (heat treatment) can effectively overcome this problem<sup>[3-5]</sup>. The fatigue resistance of material decreases with the increase in surface roughness<sup>[6]</sup>. Generally, it is accepted that the impact of the surface quality can be ignored when it meets certain requirements (e. g., surface roughness  $R_a < 0.6 \mu\text{m}$ )<sup>[7]</sup>.

Defects (voids, impurities, lack of fusion (LoF), microcracks, etc) are the more major causes for the lower fatigue life of AM alloys than conventional ones<sup>[8-9]</sup>. The location, dimension and geometry of the defects can affect the fatigue resistance by different levels. According to the research, the defects located on the surface and near the surface, as well as defects with larger size or irregular geometry (i. e., LoF and micro-crack) are more detrimental to the fatigue performance<sup>[10-14]</sup>. The mechanism of interior defect induced crack initiation and early growth of AM Ti64 alloys is attributed to the formation of nanograins caused by

Received date: September 04, 2024

Foundation item: National Natural Science Foundation of China (12172292, 12072287)

Corresponding author: Huang Wei, Ph.D., Professor, School of Aeronautics, Northwestern Polytechnical University, Xi'an 710072, P. R. China, Tel: 0086-29-88493091, E-mail: huangwei@nwpu.edu.cn

Copyright © 2025, Northwest Institute for Nonferrous Metal Research. Published by Science Press. All rights reserved.

dislocation interaction under multiple cyclic loadings, followed by cracks in combination with the cracks formed at defects,  $\alpha$  phase, interfaces, etc<sup>[15]</sup>. The porosity can be reduced by changing the scanning strategy<sup>[16-17]</sup>, optimizing the processing parameters<sup>[18]</sup> or hot isostatic pressure<sup>[13]</sup>.

During the printing process, sharp temperature gradients and low solidification velocity may cause macroscopically epitaxial columnar prior- $\beta$  grain growth along the deposition direction, leading to anisotropic mechanical properties of the workpiece<sup>[19-20]</sup>. The directional microstructural differences give rise to different fatigue resistance behavior. For low  $\Delta K$  (stress intensity factor range) fatigue crack growth (FCG) rate, it is mainly affected by the grain size and direction between crack and  $\beta$  columnar grain. FCG rate is faster when the cracks propagate along the  $\beta$  columnar, whereas it is slower when the cracks propagate perpendicular to columnar  $\beta$  grain<sup>[21]</sup>. The former researches suggest that the microstructural features dominate the early stage of crack nucleation and propagation<sup>[22]</sup>. The small crack effect (crack propagates under the threshold value of long crack with a high FCG rate under conditions of the same stress intensity factor range) was also found in AM Ti64<sup>[23]</sup>. In general, equiaxed  $\alpha$  phase is often regarded as the potential origin of fatigue crack due to its brittleness<sup>[24]</sup>. The basket weave microstructures are conducive to the promotion of tensile strength and ductility<sup>[22,25-26]</sup>;  $\alpha$  laths with great thickness and  $\alpha$  colonies have been demonstrated to be effective microstructures that restrict crack propagation and favor fracture toughness improvement of titanium alloys<sup>[27-30]</sup>.

Previous researches on AM Ti64 are mainly focused on fatigue life and long crack growth behavior with intact surface. However, in actual service requirements, AM parts inevitably encounter geometries such as notches, holes and grooves. The presence of these stress-concentrated areas may accelerate damage accumulation and threaten structural safety. Moreover, the crack initiation process and the early propagation process consume the vast majority of the total fatigue life of titanium alloys<sup>[31-32]</sup>. Therefore, the nucleation and early crack propagation behavior are crucial for the application of AM Ti64 in inclusive and safe design. For now, however, the relevant studies are comparatively rare. Wu et al<sup>[23]</sup> studied the small FCG behavior of selective laser melted Ti64 and found that it has a small crack effect and crack closure effect. The small crack tends to grow along the  $\alpha$  lath or  $\alpha/\beta$  interface and is restricted by  $\alpha$  grain boundary ( $\alpha_{GB}$ ). Liu et al<sup>[33]</sup> investigated the interior defect-induced crack initiation mechanism and early growth behavior of Ti64 manufactured by laser powder bed fusion (LPBF). Their study suggests that the fine-grained area in LPBF Ti64 is composed of numerous discontinuous nanograins responsible for grain refinement, which is associated with dislocation movement within the martensitic laths. The microvoids formed by both the fatigue loading process and the LPBF process merge and are aggregated with each other, accelerating the propagation of microcracks. It is noteworthy that there are complex interactions between various defects and grain structures, which is

essential to establish the qualitative and quantitative relationships between microstructure and engineering performance of materials. In-situ investigation arose to adjust such requirement, i. e., in-situ scanning electronic microscope<sup>[34-36]</sup> synchrotron radiation X-ray microtomography<sup>[37]</sup> and in-situ electron backscatter diffraction<sup>[38-39]</sup>.

In this study, four-point bending test with SE(B) U-notch specimens machined by wire electrical discharge was employed to investigate the crack initiation and early propagation behavior of LMD Ti64. The microstructural analysis was also conducted to further explicate the mechanism. The study aims to draw instructive conclusions for the security evaluation of AM Ti64, and further reveals the connection among special microstructural features, crack initiation and early propagation.

## 1 Experiment

### 1.1 Material

The as-received LMD Ti64 was manufactured by Xi'an Bright Laser Technologies Co., Ltd, China. The workpiece was fabricated directly on a substrate of forged annealed Ti64 titanium alloy with Ti64 powders (40–178  $\mu\text{m}$  in diameter), which were dried below 120  $^{\circ}\text{C}$  in vacuum beforehand. The chemical composition of LMD Ti64 is listed in Table 1. As for the manufactured processing, the printing used an alternating strategy: the laser path was rotated by 180 $^{\circ}$  for each consecutive pass within the same layer, and turned by 90 $^{\circ}$  for the neighboring scanning layer, as shown as Fig. 1a. The fabrication was performed in a protective argon atmosphere to avoid oxidation. A comparatively high laser power and overlap ratio were adopted to further reduce defect formation in the workpiece<sup>[1,40]</sup>. This, in turn, leads to epitaxial columnar grain growth<sup>[34]</sup> and low volume fraction of martensitic<sup>[41]</sup>. The processing parameters are listed in Table 2. Heat treatments were carried out for residual stress relieving and plasticity improving<sup>[22]</sup>, as shown in Fig. 1b. The workpiece was firstly subjected to solid solution treatment in the vacuum heat treatment furnace. The temperature slowly increased to 920  $^{\circ}\text{C}$  and was held for 2 h. Thereafter, gas quenching was carried out till the temperature decreased to 540  $^{\circ}\text{C}$ , which was held for 4 h for aging treatment, followed by air cooling to room temperature. Finally, LMD Ti64 bulk with dimensions of 110 mm $\times$ 105 mm $\times$ 130 mm was obtained, as shown in Fig. 1c.

The as-received LMD Ti64 was measured by tomoscanner YXLON MU2000-D, and the porosity was calculated to be 0.097% by Dragonfly 4.0<sup>[42]</sup>. The violent heat exchange may lead to the formation of defects<sup>[40]</sup>. Therefore, defects are prone to form in the near external surface of the bulk, where the heat exchange is more violent. In contrast, defects are hardly found in the interior of LMD Ti64 bulk where the heat

**Table 1 Chemical composition of as-received LMD Ti64 (wt%)**

Al	V	Fe	Si	C	N	H	O	Ti
6.02	4.00	0.098	0.033	0.025	0.04	0.008	0.16	Bal.

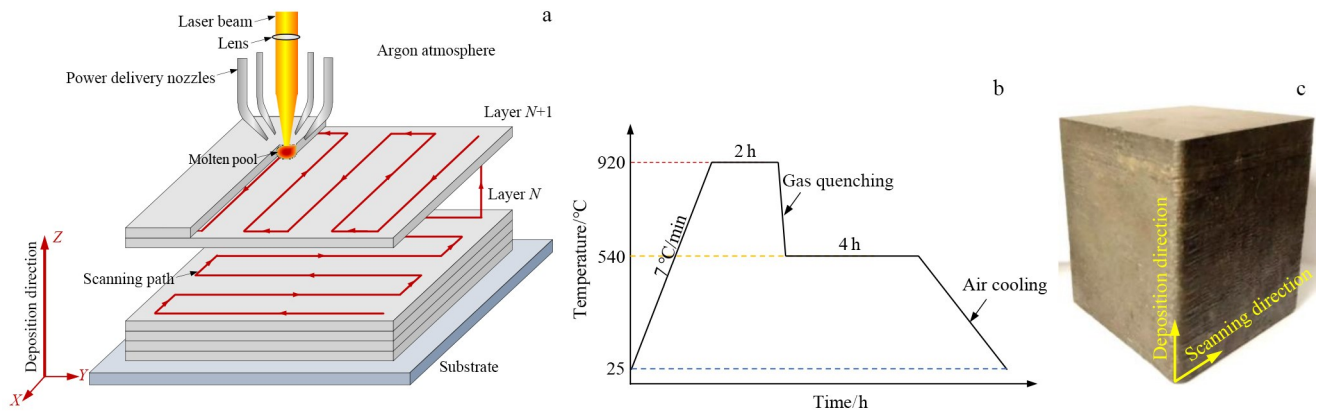


Fig.1 Schematic diagrams of LMD Ti64 printing process (a), history of heat treatment (b), and as-received bulk of LMD Ti64 (c)

Table 2 LMD processing parameters

Laser type	Laser power/kW	Scanning velocity/mm·s <sup>-1</sup>	Powder feeding rate/g·min <sup>-1</sup>	Overlap ratio/%
Fiber optic laser	7	12–15	15–30	30–50

exchange is placid. The microstructure of the interior of the bulk is shown in Fig.2. The printing strategy also leads to epitaxial columnar grain growth<sup>[34]</sup> and thus low volume fraction of martensitic<sup>[41]</sup>. In building direction (plane  $XOZ$ ), there are a large columnar prior- $\beta$  grain ( $\beta$  grain) with 0.5–2 mm in width and 2–5 mm in length. The growth direction of the columnar grains is not definitely parallel to the deposition direction, with small angles of 8°–15°. This is related to the molten pool geometry and the optimal direction of heat dissipation to the substrate<sup>[25]</sup>. The microstructure in scanning direction (plane  $XOY$ ) is presented as equiaxed grain (Fig.2a). These grain size range from 100  $\mu\text{m}$  to several hundreds of microns. With a greater magnification, (Fig.2c), as the columnar grains are cut along the scanning direction in plane  $XOY$ , the characteristic grain size is smaller than that in  $XOZ$  plane. Higher grain boundary density forces the fatigue crack to break through

more energy barriers during the propagation process, and hence a better fatigue resistance is found in the building direction for the long crack growth<sup>[7]</sup>. In plane  $XOZ$  (Fig.2d), substantial  $\alpha$  laths, with 10–100  $\mu\text{m}$  in length and 2–5  $\mu\text{m}$  in thickness, parallel to each other can be observed along  $\beta$  grain boundary. These clustered  $\alpha$  laths constitute a colony of  $\alpha$  laths ( $\alpha$  colony), which may stretch along the  $\beta$  grain boundary by hundreds of microns. The shorter  $\beta$  grain boundary in plane  $XOY$  reduces the occurrence probability of  $\alpha$  colony. It can be found that in plane  $XOY$ , obvious basket weave microstructure and coarser  $\alpha$  laths with large thickness appear, as shown in Fig.2e. The basket weave interspersed with equiaxed  $\alpha$  phases with diameter ranging from 5  $\mu\text{m}$  to 30  $\mu\text{m}$  is observed in both planes  $XOY$  and  $XOZ$ , as shown in Fig.2d–2e.

## 1.2 Specimen and test

To cover different situations, specimens in three directions

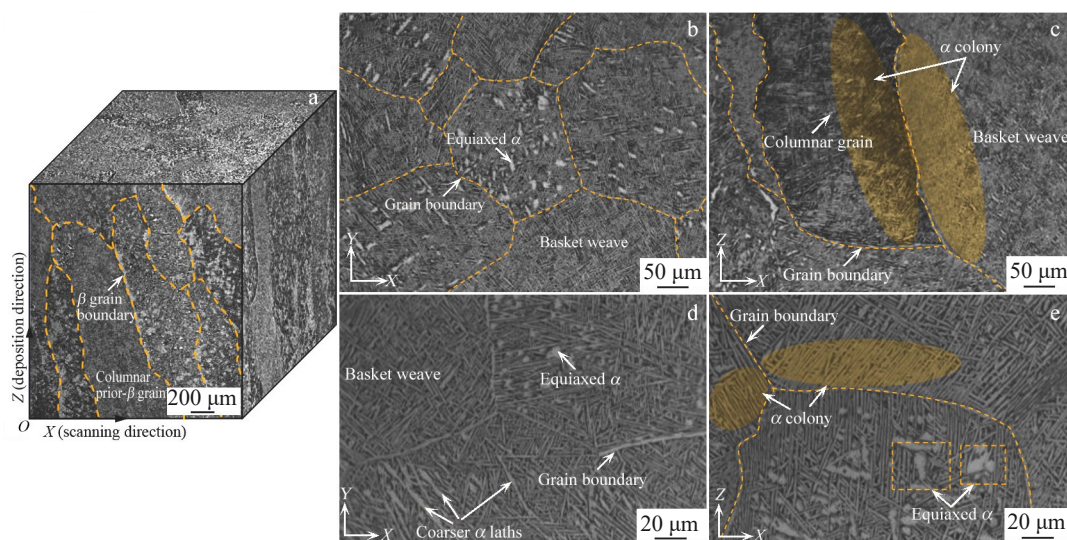


Fig.2 Microstructure characterization of LMD Ti64 in different directions: (a) overall view, (b, d)  $XOY$  plane, and (c, e)  $XOZ$  plane

were employed to investigate the fracture response of LMD Ti64. In order to minimize the influence of defects on the dispersion of fatigue test, all the specimens were processed with the materials inside the bulk. The specimen with crack plane parallel to the deposition direction or extending along the deposition direction is defined as *X*-direction (XD), *Y*-direction (YD) and *Z*-direction (ZD) specimens, as shown as Fig.3a. The conventionally forged Ti64 specimens were also introduced for comparison. A notch of about 0.5 mm was processed on each specimen by low-speed wire electrical discharge machining (EDM), and diameter of wire was 0.2 mm. The diameter of the semicircular EDM notch of specimens was kept within 0.2–0.25 mm, and the machining error of notch length was kept within  $\pm 0.1$  mm. The surface roughness was tested by MarTalk surface quality testing machine. The mean value of the average surface roughness ( $R_a$ ) was calculated to be 0.478  $\mu\text{m}$ . The surface roughness was not considered.

Four-point bending fatigue tests were conducted on an electro-hydraulic servo fatigue testing machine (Instron 8801). Fig.3b shows the geometric dimensions of the specimen, the length of the notch obtained after EDM is marked as  $a_0$ , and the length of fatigue crack which occurs after a certain period is marked as  $a_f$ . As shown in Fig.3c, all indenters are 2.5 mm in radius, the upper ones are 6 mm apart, and the lower ones are 20 mm apart. The relative position of the indenters and the pre-existing EDM notch should be identical to assure a consistent loading condition. The tests adopted load control mode (constant amplitude stress, accuracy  $\pm 1\%$ ) and sinusoid signal input with a stress ratio of 0.1 and a frequency of 50 Hz. The maximum load of the fatigue test was selected as about 75% of the yield strength  $\sigma_{0.2}$ , i. e.,  $\sigma_{\max} = 600$  MPa. In order to accurately observe the initiation and propagation history of fatigue crack, Suolan50-1000x microscope with a maximum magnification of 1000 $\times$  was engaged to simultaneously monitor and record the whole process. By visualization of the history of crack propagation, the relation between loading cycles and crack length can be obtained.

### 1.3 Microstructure characterization

OLYMPUS OLS-4000 optical microscope (OM), JSM-IT700HR scanning electron microscope (SEM) equipped with

electron backscattered diffraction (EBSD) detector and Aztec acquisition software were used for the subsequent microstructure and fractography analysis. The specimens were successively ground and polished with alumina suspension, and surface was etched by Kroll's reagent (1 mL HF+3 mL HNO<sub>3</sub>+100 mL H<sub>2</sub>O) for 60 s. The EBSD specimens were prepared by electropolishing in a solution consisting of perchloric acid and absolute ethyl alcohol (volume fraction ratio of 15:85) at 20 V for 30 s.

## 2 Results and Discussion

### 2.1 Crack early propagation velocity

Fig. 4 illustrates typical crack propagation history of LMD Ti64 specimen (X11). Based on the relationship between the crack length ( $a$ ) and the number of cycles ( $N$ ) recorded in the fatigue test, the  $a$ - $N$  curves of forged Ti64 specimens (F1–F13) and LMD Ti64 specimens in XD (X1–X24), YD (Y1–Y15) and ZD (Z1–Z15) are shown as Fig.5.

Due to small size of the specimens used in this research, the lengths of cracks are less than 2 mm in total. At such a small distance, the probability of encountering the grain boundary will be greatly reduced during the crack propagation process. Instead, the randomly distributed  $\alpha$  colony,  $\alpha$  laths and other microstructural features dominate the early crack propagation, as well as the propagation velocity. Therefore, to avoid the loss of information caused by irregular fluctuations of FCG rate in the low  $\Delta K$  region, the  $a$ - $N$  curves were used in this study rather than  $da/dN$ - $\Delta K$  diagram. All the scatter diagrams are normalized in median value, as shown as Fig.6. Although the  $a$ - $N$  curves show dispersion in a certain range, they still tend to be linear overall. Compared with LMD Ti64 specimens, the forged specimens are significantly less dispersed. During the early stage, the crack propagates with a step-like tendency. The presence of  $\alpha$  laths and other features retarding the crack propagation, or the crack closure induced by plasticity, gives rise to the platforms of the curves<sup>[23]</sup>. The crack propagation velocity of the vast majority of specimens is concentrated at  $2 \times 10^{-8}$ – $3 \times 10^{-8}$  m/cycle, which indicates that the LMD Ti64 has a typical small crack effect.

### 2.2 Crack initiation

Due to good plasticity of Ti64, attention should be paid to

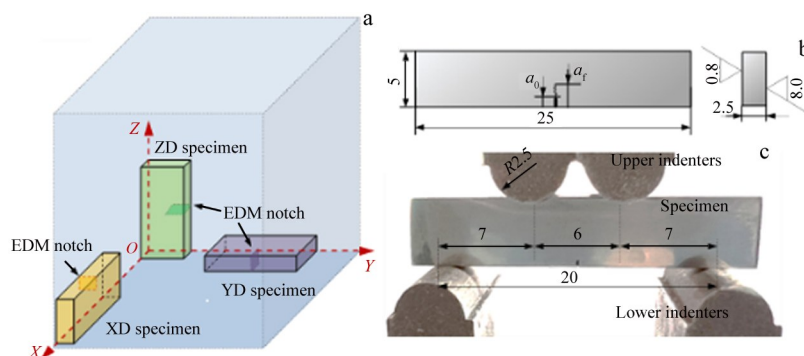


Fig.3 Schematic illustrations of LMD Ti64 specimens in different directions (a), geometry of specimen (b), and configuration of four-point bending test (c)

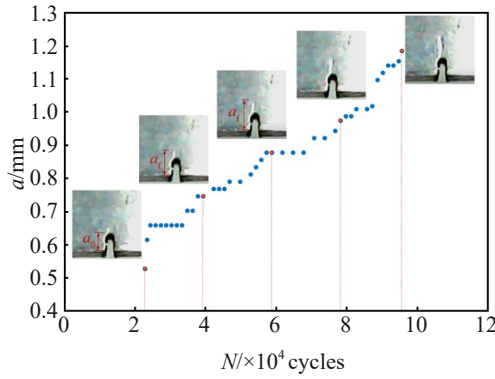


Fig.4 History of crack propagation of X11 LMD Ti64 specimen

the plastic zone changes caused by damage accumulation when determining the moment of crack initiation. The crack initiation cycle numbers of four different specimens under the same loading conditions are tallied, with 10 intervals and increments of 10 000, from 0 to 100 000 cycles. As can be seen from Fig. 7, the distribution of forged Ti64 is not obviously regular, while LMD Ti64 specimens in XD, YD and ZD all follow logarithmic normal distributions. A mathematical model can be used to fit:

$$f(x) = \frac{A}{\sqrt{2\pi}\omega x} e^{-\frac{\left(\ln \frac{x}{x_c}\right)^2}{2\omega^2}} \quad (1)$$

where  $A$ ,  $\omega$  and  $x_c$  indicate the area, log standard deviation and center of logarithmic normal distribution, respectively; The mean  $\mu$  and standard deviation  $\sigma$  can be given by

$$\mu = e^{\ln x_c + (\omega^2/2)} \text{ and } \sigma = e^{\ln x_c + (\omega^2/2)} \sqrt{e^{\omega^2} - 1}, \text{ respectively.}$$

The distribution parameters are roughly similar in value, except for  $A$ . The reason for the huge difference in the value of  $A$  is the difference in sample capacity. As listed in Table 3, the basically consistent value of log standard deviation  $\omega$ , center  $x_c$ , mean  $\mu$  and standard deviation  $\mu$  indicates that there is no obvious difference in the fatigue crack initiation of XD and YD specimens. As for ZD specimen, the values of  $\omega$  and  $\sigma$  are far less than those for XD and YD specimens, and its crack initiation cycle number distribution is more concentrated. Most of the ZD specimens have higher initiation cycles than the other two specimens, referring to more microstructural features hindering crack nucleation in the fracture section of ZD specimens.

To better evaluate the crack initiation and early propagation behavior of LMD Ti64, the crack initiation position angle  $\theta_p$  and crack initiation direction angle  $\theta_d$  are introduced. The coordinate system of  $\theta_p$  is established with the center of the semicircular EDM notch as origin. The coordinate system of  $\theta_d$  is established with the center of the semicircular EDM notch as origin.  $\theta_p$  indicates the angle between  $X$ -axis and the line connecting the origin and crack initiation position, as shown by the red arrows in Fig. 8a. With the crack initiation position as origin, the angle between the crack early propagation path and the  $X$ -axis which is perpendicular to the loading direction is defined as the crack early propagation direction angle  $\theta_d$ , as shown by the yellow arrows in Fig. 8a. For the part of specimens with multiple cracks, only the main cracks are counted.

The crack initiation position angles of each specimen are

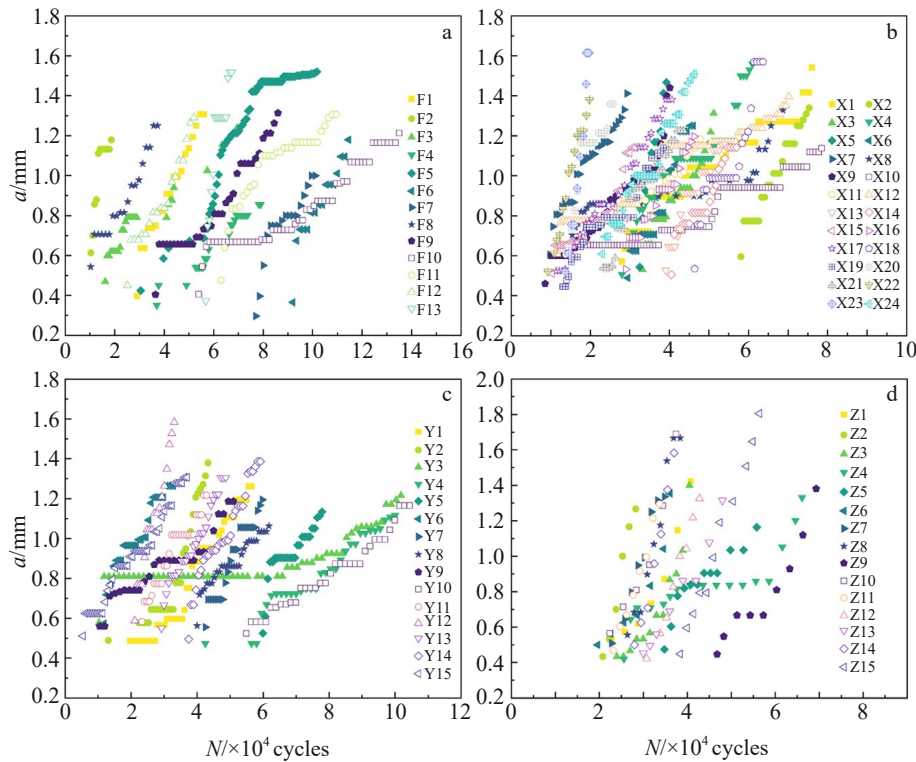


Fig.5  $a$ - $N$  curves of forged Ti64 specimens (a) and LMD Ti64 specimens in XD (b), YD (c), and ZD (d)

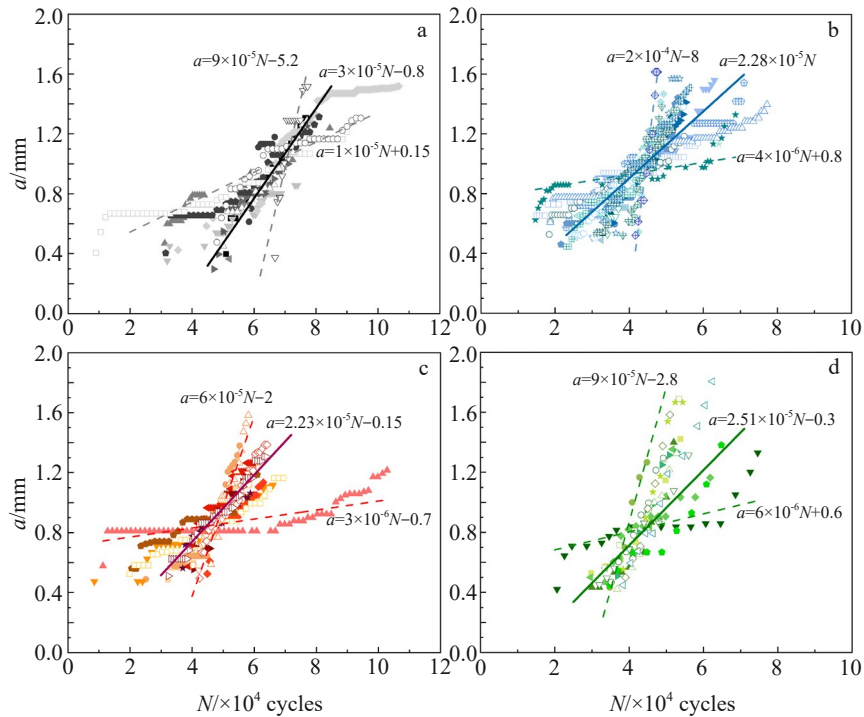


Fig.6 Crack early propagation rate of forged Ti64 specimens (a) and LMD Ti64 specimens in XD (b), YD (c), and ZD (d)

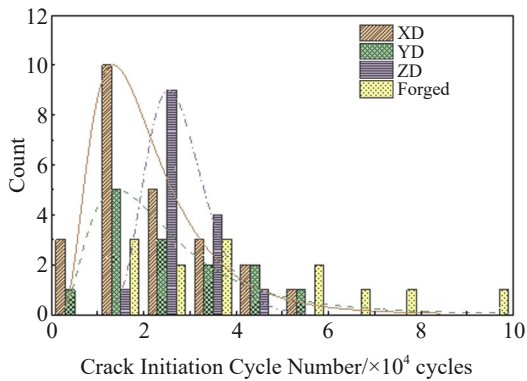


Fig.7 Distribution of crack initiation cycle numbers of different specimens

Table 3 Logarithmic normal distribution parameters of crack initiation cycle numbers of different specimens

Specimen	Parameter				
	$A/\times 10^4$	$\omega$	$x_c$	$\mu$	$\mu$
XD	24	0.563 18	18 501.1	21 680.6	13 245.3
YD	14	0.640 17	21 415.7	26 286.0	18 708.3
ZD	15	0.242 56	26 960.7	27 765.6	6 835.1

counted in increment of  $10^\circ$ . Fig. 8b shows that the forged Ti64 specimens have very little dispersion and little offset, only  $90^\circ \pm 10^\circ$ . In contrast, the anisotropy of LMD Ti64 and its microscopic features make the crack initiation position significantly more dispersed than that of the forged ones. The XD, YD and ZD specimens in the interval of  $90^\circ \pm 10^\circ$  account

for 45.83%, 60% and 66.67%, respectively. The maximum deviation of the cracking position is within  $90^\circ \pm 45^\circ$ . Among them, the cracking position of the AM specimens has different degrees of dispersion, and XD specimen has the most dispersed cracking position, followed by YD and ZD specimens. Although the cracking sites are scattered, they are all between  $90^\circ \pm 45^\circ$ . That is affected by both loading direction and the microstructural characteristics of LMD Ti64. There will be some dispersion for crack initiation position. However, they still basically follow the normal distribution. The crack initiation direction angles are also counted in increment of  $10^\circ$ , from  $70^\circ$  to  $140^\circ$ . As shown in Fig. 8c, the dispersion of the forged specimens is still significantly less than that of the LMD ones. For the forged specimens, all of the crack early propagation angles are in the interval of  $90^\circ \pm 10^\circ$ . While for the LMD Ti64 in XD, YD and ZD, the percentage of specimen falling in  $90^\circ \pm 10^\circ$  is 79.17%, 93.33% and 86.67%, respectively. Most of the remaining specimens fall in the interval of  $90^\circ \pm 20^\circ$ . Among them, XD specimen with a crack early propagation angle up to  $130^\circ$  is also found.

As shown in Fig. 9a, some of the specimens have multiple cracks, which are distributed on the edge of the U-notch. These cracks compete with each other, and the winner eventually grows into the main crack. For the uniformly forged Ti64, the crack initiation point is basically only affected by the external force, so the nucleation always happens around the central point of the semicircular notch edge. As for LMD Ti64, due to its random microstructure distribution, the crack initiation position roughly follows a normal distribution. As shown in Fig. 9b and 9c, when the  $\beta$  grain boundary appears on the semicircular edge of notch, it is

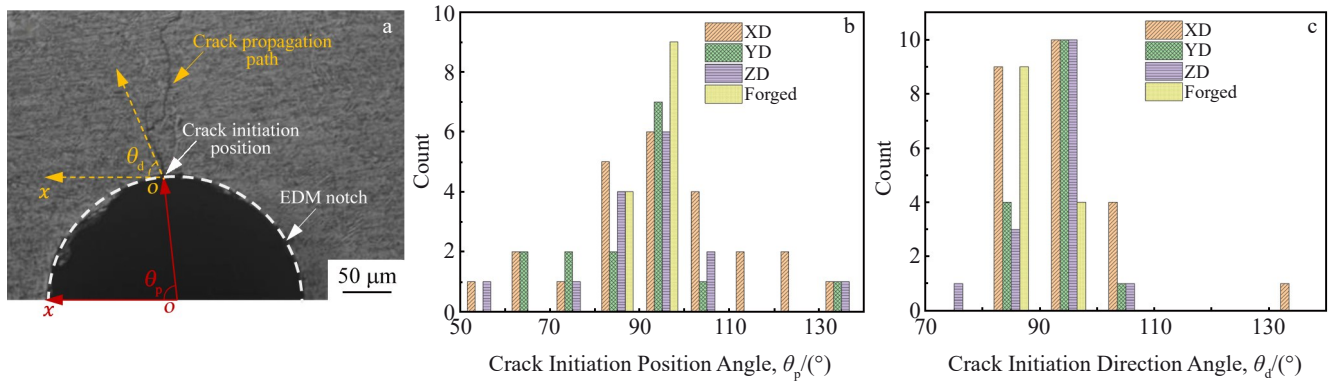


Fig.8 Schematic of crack initiation position angle  $\theta_p$  and crack early propagation direction angle  $\theta_d$  (a); distribution of  $\theta_p$  (b) and  $\theta_d$  (c) in forged Ti64 and LMD Ti64 specimens

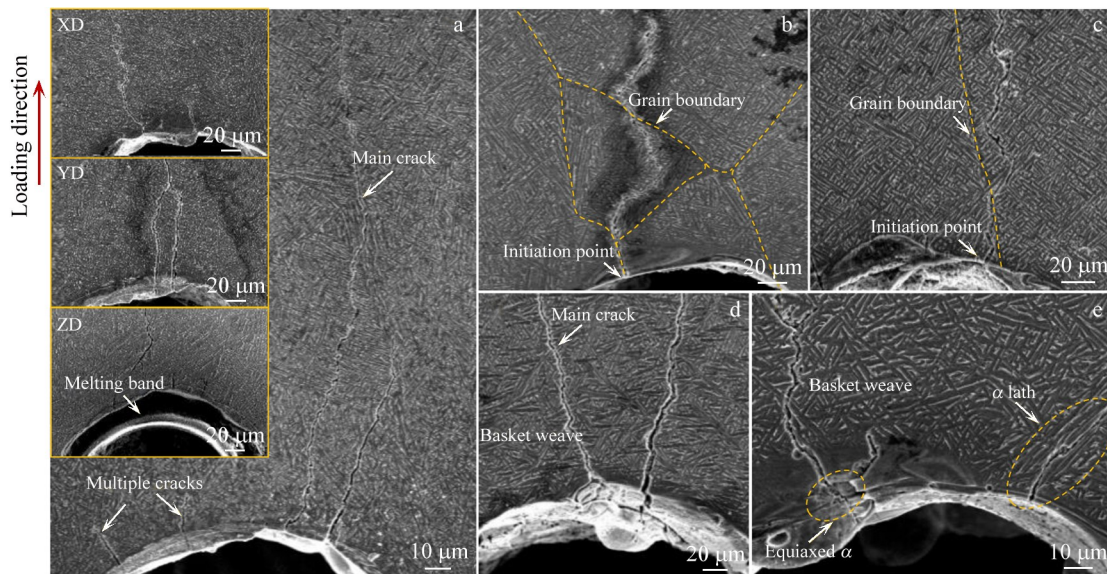


Fig.9 SEM images of crack initiation position: (a) multiple cracks, (b–c) at the grain boundary, (d) within basket weave structure, and (e) at equiaxed  $\alpha$  and around 45° to  $\alpha$  laths

always found to be the crack initiation point. This is also one of the reasons for the deviation of crack initiation position angles from the center (90° crack initiation position angle). When the semicircular edge of notch is surrounded by the uniform basket weave structure, the cracks are prone to nucleate at the center under the action of external forces (Fig.9d). Besides, it is also found that the cracks are initiated at the site of enriched equiaxed  $\alpha$  or around a little bunch of parallel  $\alpha$  laths (Fig.9e). Theoretically, cracks nucleate at the site with the lowest energy barrier. The presence of U-notch will cause stress concentration on the edges, and the stress concentration may provide free surfaces for cyclic slip of material. Under the combined action of external forces and the microstructure, cracks tend to initiate and propagate in the favorable grains for slip, such as the grain boundary,  $\alpha/\beta$  interfaces and equiaxed  $\alpha$ . Issues related to the slip system are mentioned in detail in the following section.

### 2.3 Early propagation behavior

Fig. 10 shows the early propagation paths and fracture

surfaces of the forged Ti64 and LMD Ti64 specimens, and their macroscopic sections are in the upper right corner. Overall, the crack growth direction of forged Ti64 coincides with the loading direction. There is almost no occurrence of deflection, multiple cracks or secondary cracks on the paths. Correspondingly, the fracture of forged Ti64 is flat. In contrast, affected by the microstructure characteristics of LMD Ti64, varying degrees of deflection happen in the process of crack growth along XD, YD and ZD, finally resulting in zig-zag crack propagation paths. Multiple cracks and secondary cracks are commonly found.

The fracture surfaces of forged specimen and LMD specimens along XD, YD and ZD are shown in Fig.11. Forged Ti64 is a typical dual phase titanium alloy, with uniformly distributed  $\alpha$  phase and  $\beta$  phase. Compared with the LMD Ti64 specimens in all directions, the fracture surfaces of forged Ti64 have uniform dimples overall and exhibit a sponge-like appearance, which indicates a typical ductile fracture<sup>[43–44]</sup>. No obvious secondary cracks are observed. The

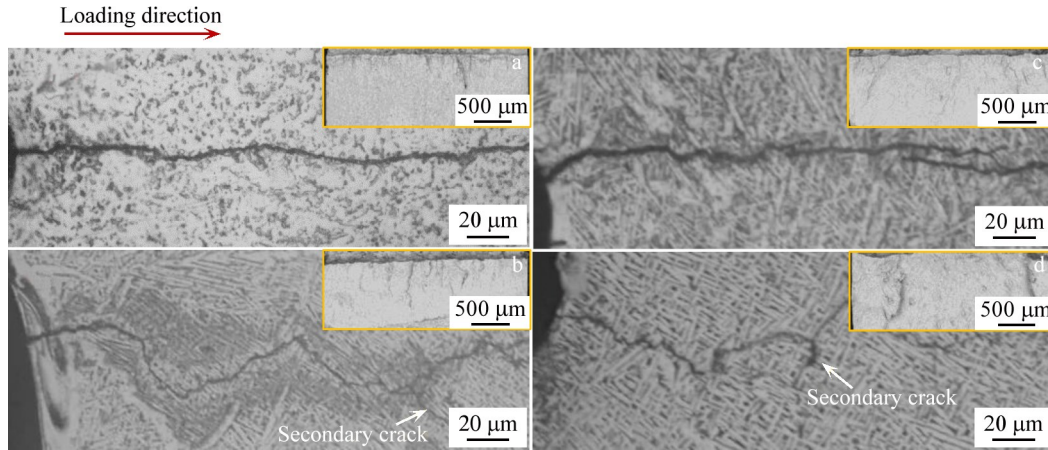


Fig.10 OM images of crack early propagation path of different specimens: (a) forged, (b) XD, (c) YD, and (d) ZD

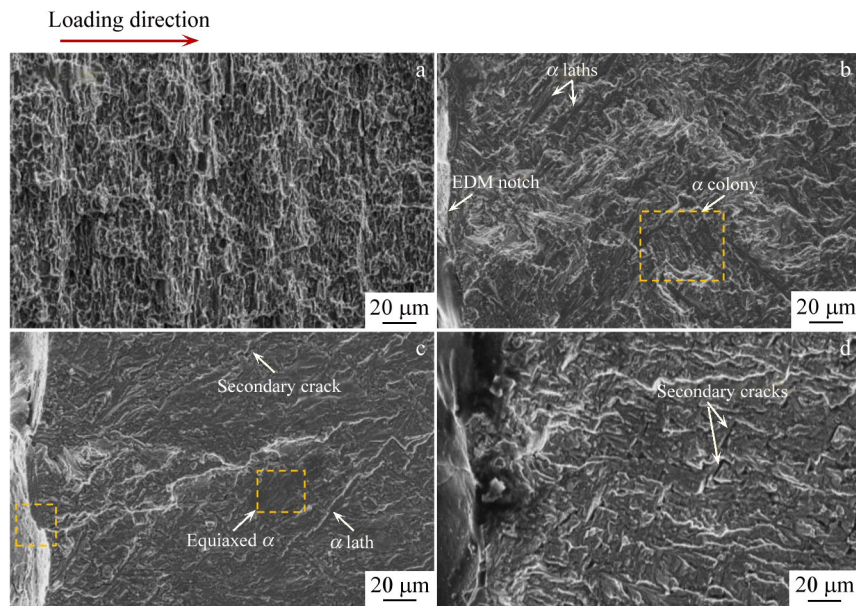


Fig.11 Fracture surfaces of forged specimen (a) and LMD specimens in XD (b), YD (c), and ZD (d)

fracture surfaces of LMD specimens are relatively rough, with ridge-like morphology. The strips and little facets left by  $\alpha$  laths and  $\alpha$  colonies are observed. The relatively smooth small facet left by equiaxed  $\alpha$  is occasionally found. There are a large number of secondary cracks on the fracture surfaces. In contrast with XD and YD specimens, ZD specimen have obviously more intensive secondary cracks.

Previous studies have shown that the high cycle fatigue strength, which refers to the resistance to crack nucleation, depends primarily on the first dislocation motion and the yield stress in most cases. Similarly, as described for the macrocracks, the fracture toughness of dual phase titanium alloys usually increases with increasing the colony size because the rougher crack front profile dominates over the ductility term<sup>[43]</sup>.

The slip characteristics of materials, the scale of microstructure, the stress level and the size of plastic zone near the crack tip have a strong influence on the microscopic

mode of fatigue crack propagation. For ductile metals, the FCG caused by cyclic loading can be regarded as the process of abrupt local deformation in the macroscopic plastic zone at the crack tip. The plastic zone at fatigue crack tip plays a crucial role in fatigue crack propagation. The plastic zone at the fatigue crack tip can be divided into unidirectional plastic zone and cyclic plastic zone. The unidirectional plastic zone is generated by the far-field load, and changes with the load. The cyclic plastic zone is the reverse flow deformation region generated when the far-field load changes. Under plane stress conditions, the size of the unidirectional plastic zone  $r_p$  and the size of the cyclic plastic zone  $r_c$  can be calculated by the following formula<sup>[45]</sup>:

$$r_p = \frac{1}{\pi} \left( \frac{K_{\max}}{\sigma_y} \right)^2 \quad (2)$$

$$r_c = \frac{1}{\pi} \left( \frac{\Delta K}{2\sigma_y} \right)^2 \quad (3)$$

where  $K_{\max}$ ,  $\Delta K$  and  $\sigma_y$  indicate the maximum stress intensity factor, the stress intensity factor range and yield stress, respectively. According to the formula, both unidirectional plastic zone and cyclic plastic zone are related to the yield strength of the material surrounding the instant crack tip. For example, when the  $\alpha$  laths and adjacent  $\beta$  phases undergo plastic deformation, large coordinated deformation region will appear. The  $\alpha$  phase and  $\beta$  phase with different slip systems have the Burgers' orientation relationship. When the dislocation in  $\alpha$  or  $\beta$  phases moves to the phase interface, it can enter other phases with small energy resistance, thus forming a long-range slip through the  $\alpha$  laths. The large coordinated deformation region around  $\alpha$  lath and the easily initiated long-range slip make it prone to form a large range of plastic deformation, which then leads to more deflection in the crack path. That is, during the early stage of crack propagation, the microstructure in the small region ahead of the crack tip is the main factor affecting the crack propagation path.

As shown in Fig. 12, for the forged Ti64 with fine and smooth equiaxed  $\alpha+\beta$  microstructures, the blunt of the crack tip is unlikely to happen during the propagation process. As a result, the driving force generated by the cyclic loading dominates the crack propagation direction, and the plastic zone is small. It manifests as the straight crack propagation path and the smooth fracture surface, as shown in Fig. 10. The large coordinated deformation area and the long-distance slip provide conditions for the plastic deformation in a large range, which leads to the large plastic area of the crack tip within the structures of  $\alpha$  colony. Within the structures of basket weave, which is smaller and thinner than the  $\alpha$  lath and  $\alpha$  colony, the surrounding coordinated deformation area is also smaller during plastic deformation. They are more uniform in size and have different slip directions, which may restrict the long-distance sliding. Therefore, the plastic zone will be smaller

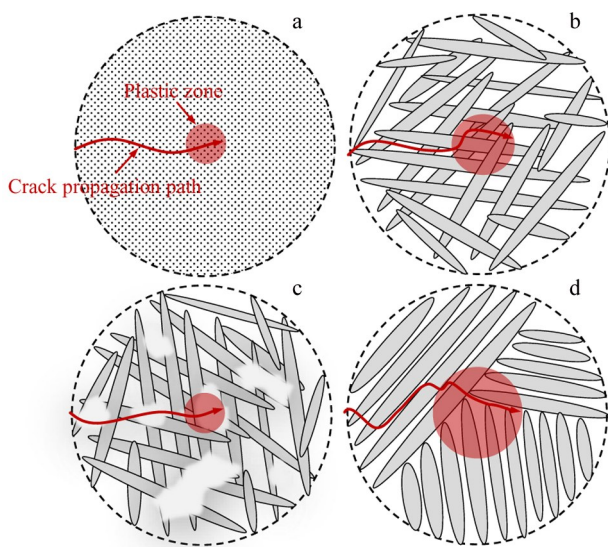


Fig.12 Coordinated deformation area and plastic zone size of different microstructures: (a) equiaxed  $\alpha+\beta$ , (b) basket weave, (c) equiaxed  $\alpha$ , and (d)  $\alpha$  lath

than that of  $\alpha$  colony. Equiaxed  $\alpha$  is the brittle phase in LMD Ti64. When the crack tips go through equiaxed  $\alpha$ , the driving force for crack propagation will degrade at once. In this process, the cracks propagate quickly and a relatively flat facet is left on the fracture surface.

According to SEM observation, the dark  $\alpha$  phase has a dominant influence on the crack propagation path which is always parallel and perpendicular to the  $\alpha$  lath, consistent with the previous findings<sup>[46-47]</sup>. As shown in Fig. 13a and 13b, when the crack passes through an  $0^\circ$   $\alpha$  colony and  $90^\circ$   $\alpha$  lath, the crack propagation direction remains consistent with the loading direction, and basically no deflection occurs. In the crack path of  $0^\circ$   $\alpha$  colony, the short secondary cracks will always appear on both sides of the main crack. However, when encountering tilted  $\alpha$  colony, the crack is prone to deflect with large angles and long-distance slip, as shown in Fig. 13c. When multiple tilted  $\alpha$  laths are distributed ahead of the crack, the crack propagation direction will be continuously bent, forming a path shown in Fig. 13d. When the aggregation of thick  $\alpha$  laths occurs in front of the crack, the propagation will be blocked due to the restriction of the coordinated deformation of the plastic region, which then changes the propagation direction, as shown in Fig. 13e. The  $\alpha_{GB}$  also hinders the crack propagation (Fig. 13f), and the crack is deflected after encountering the  $\alpha_{GB}$ . In addition, when the crack passes through the basket weave area, within which the thin and short strip  $\alpha$  crisscrosses (Fig. 13g), it leaves a zig-zag path and secondary cracks in the position where the direction is greatly changed. The brittle equiaxed  $\alpha$  with low strength is a good choice of crack propagation path. As shown in Fig. 13h, the crack avoids the basket weave with higher strength in the right front and extends along the aggregation of equiaxed  $\alpha$  edge under external force. When encountering small defects with irregular shape, the cracks tend to extend along the sharp corner of stress concentration (Fig. 13i).

Fig. 14 shows schematics of crack paths<sup>[47]</sup>. For dual phase titanium alloys, there is a Burgers' relationship between the  $\alpha$  phase (hexagonal close-packed structure, hcp) and the  $\beta$  phase (body-centered cubic, bcc), which is  $(110)_\beta // (0001)_\alpha$  and  $(111)_\beta // \langle 11\bar{2}0 \rangle_\alpha$ <sup>[48]</sup>. The crack initiation, early and stable propagation stages appear to be dominated by the same shear activity. The dislocations accumulate at  $\alpha/\beta$  interfaces until the barrier breakdown takes place and then drives the shear band to propagate. The crack tip is subjected to two shear modes on the  $\alpha$  basal  $(0001)$  plane and the  $\alpha$  prismatic  $\{10\bar{1}0\}$  plane. The slip on  $(01\bar{1}0)$  prism plane or in various pyramidal planes of  $\alpha$  phase may give rise to the crack propagation along the parallel direction, while along the vertical direction, it is relevant to the slip along  $(0001)$  basal plane,  $(10\bar{1}0)$  prism plane or pyramidal slip<sup>[47]</sup>. The residual dislocations in  $(01\bar{1}0)$  prism plane are smaller than those in  $(10\bar{1}0)$  prism plane.  $(01\bar{1}0)$  prism slip always impinges the  $\alpha/\beta$  interfaces with a shallow angle, while both  $(0001)$  basal slip and  $(10\bar{1}0)$  prism slips form a very large angle to this interface<sup>[45,49]</sup>. Therefore, a large number of crack paths parallel and perpendicular to the

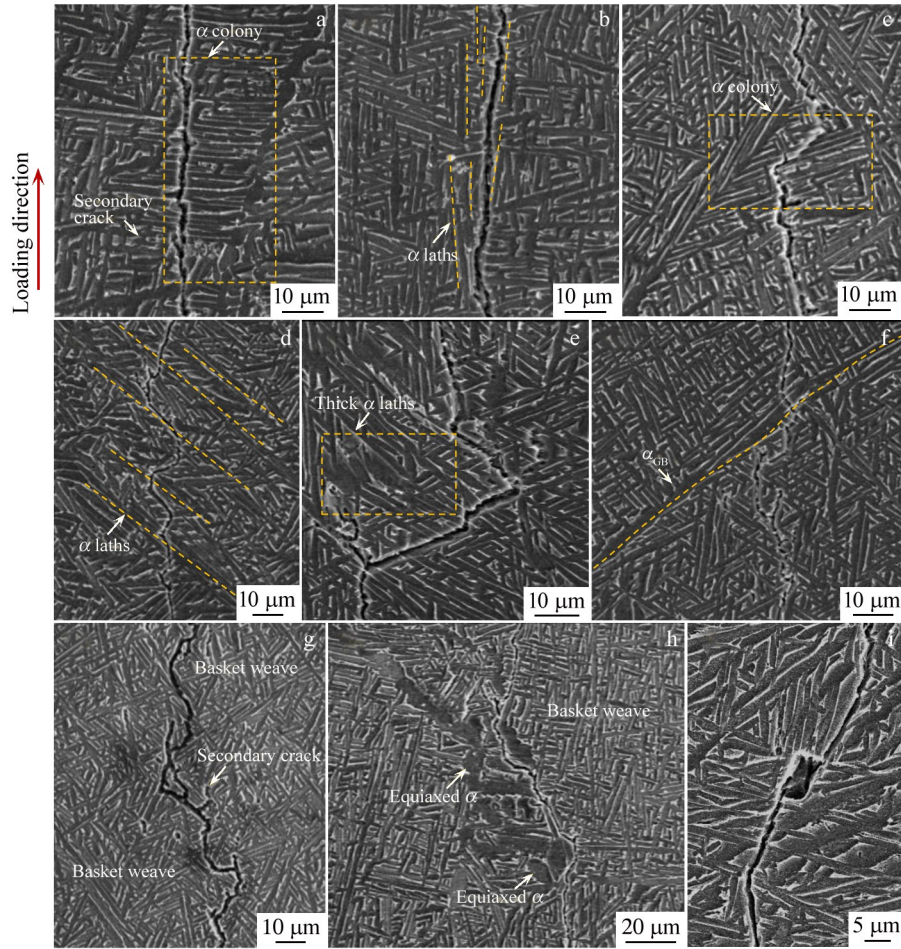


Fig.13 SEM images of crack early propagation path: (a) 0° α colony, (b) 90° α laths, (c) oblique α colony, (d) oblique α laths, (e) thick α laths, (f) α<sub>GB</sub>, (g) basket weave structure, (h) equiaxed α, and (i) LoF defect

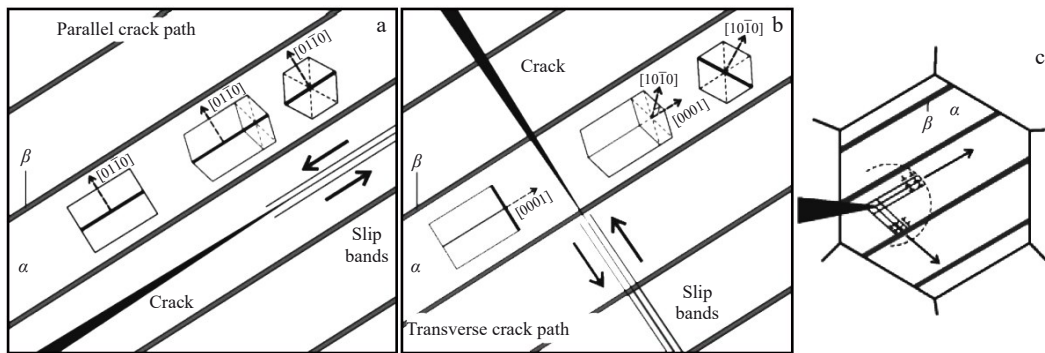


Fig.14 Schematics of parallel crack path (a) and transverse crack path (b) with respect to the orientation of the hcp α-Ti unit cell in colonies promoting perfect Burgers' relationship between α and β platelets; illustration of the slip system of α/β phase at high loading frequency (c)<sup>[47]</sup>

α laths can be observed. Li et al<sup>[50]</sup> analyzed fatigue crack initiation of AM titanium alloy TC17. Under cyclic loading, dislocations accumulate and the dislocation interaction induces grain refinement, which further increases the local microstructure inhomogeneity. By measuring the Schmid factors of different slip systems, it is found that the Schmid factors of α grains on basal plane are always higher than that

on prismatic plane. The crack initiation tends to occur within α grains due to microstructure inhomogeneity and deformation incompatibility. By a further in-situ study on AM Ti64, Chi et al<sup>[39]</sup> found that both deformation twinning and slip-induced subgrains contribute to the nanograin formation. The dislocations prefer to occur in α grains with a loading angle (between the grain and loading direction) greater than 10° ,

and the basal slips, prismatic slips and pyramidal slips are the prior slip types. While for the  $\alpha$  grains with a loading angle smaller than  $10^\circ$ , it will activate  $\{10\bar{1}2\}\langle\bar{1}011\rangle$  extension twinning for coordinating the deformation.

A large number of secondary cracks are found in the early crack propagation paths of LMD Ti64. As shown in Fig. 15, the angles between the main cracks and secondary cracks are different, and a statistic of these angles showed that the angle less than  $30^\circ$  accounts for 5.3%, the angle of about  $60^\circ$  reaches 80.2%, and the percentages of angle of about  $90^\circ$  or over  $120^\circ$  are 11.3% and 3%, respectively. The secondary cracks less than  $30^\circ$  are limited to local, usually less than  $10\ \mu\text{m}$ , without changing the growth direction of the main crack. The vast majority of the secondary cracks observed is  $60^\circ$ , and they are generally accompanied by the deflection of main cracks. As for the secondary cracks greater than  $60^\circ$ , they disperse the force on the crack tip more strongly, and may overtake the main crack and replace it.

The formation of secondary cracks can be recognized as the accumulation of dislocations at phase or grain boundaries under cyclic loading, which blunts the crack tip and tends to bifurcate the main crack. After that, it grows along fragile phase boundaries until the driving force is insufficient to make the crack propagate<sup>[51]</sup>. The activation of the slip system is generally determined by the critical resolved shear stress, and the critical resolved shear stress of prism plane is generally lower than that of the basal plane<sup>[52]</sup>. Due to the anisotropy in transmission at  $\alpha/\beta$  interfaces, the slip length along (0001) basal slip or  $(10\bar{1}0)$  prism slip is less limited than that along  $(01\bar{1}0)$  prism slip. Generally speaking, cross-slip events may occur on the premise of high critical resolved shear stress. A large slip line spacing, which means a low critical resolved shear stress, will promote the crack propagation along the preferential slip system that is parallel to the  $\alpha$  laths, as the direction perpendicular to the  $\alpha$  laths is restricted by the  $\alpha/\beta$  interfaces. However, with the increase in loading frequency, the slip events between the interfaces become more frequent. Correspondingly, the slip density increases, so does the critical resolved shear stress. Since the crack propagation process in  $\alpha/\beta$  phase is dominated by damages originating in the  $\alpha$  phase, the increased homogenization along the principal slip system in hcp microstructure provides more possibilities for the crack

propagation directions. The slip length ahead of the crack tip in the condition of high loading frequency will also be smaller than that in the condition of low loading frequency<sup>[53]</sup>. With a smaller slip line spacing, the probability of cross-slip events increases. Therefore, secondary cracks are more likely to appear in the crack propagation process under high loading frequency conditions. Note that there are two preferential crack propagation directions under high loading frequency, as illustrated in Fig. 14c. The angle between these two directions is about  $60^\circ$ , which corresponds to the results in preceding paragraphs.

#### 2.4 Effect of grain orientation

The fatigue test results suggest that grain orientation has a significant influence on crack initiation and early propagation behavior. For long cracks, the columnar  $\beta$  grain boundaries play an important role in hindering crack propagation<sup>[7]</sup>. However, for small size specimens and small cracks, the probability of the crack to encounter  $\beta$  grain boundary during its propagation process will be greatly reduced as the crack length is less than the width of  $\beta$  grain. Therefore, the growth direction of the columnar  $\beta$  grain is the main factor that controls the direction of  $\alpha$  phase and the deflection angle of the fatigue crack<sup>[54]</sup>. That is, as the growth direction of columnar  $\beta$  changes, the slip system direction will be changed. Under fatigue loading, the grains near the crack source undergo cyclic plastic deformation such as slip. The non-uniform distribution of crystallographic orientations produces various crystallographic textures, further leading to different difficulty levels of slip. The difficulty for the grains to slip during the crack initiation stage is positively related to the difficulty for the cracks to initiate and the fatigue life length. When the cooling temperature is below the  $\beta$ -transus temperature, a part of bcc  $\beta$ -Ti phase will be transformed into hcp  $\alpha$ -Ti, and this process provides twelve possibilities to the orientations of  $\alpha$  phase. The preferred orientation of the grains makes the crystallographic texture different in three directions, resulting in the anisotropy of the mechanical properties<sup>[55]</sup>. Fig. 16 shows different microstructure characteristics of LMD Ti64 in three directions. The columnar  $\beta$  grain in XD specimens is basically parallel to the crack plane, with angle of  $8^\circ - 15^\circ$  to the vertical direction. The columnar  $\beta$  grains in YD specimens are cut along the

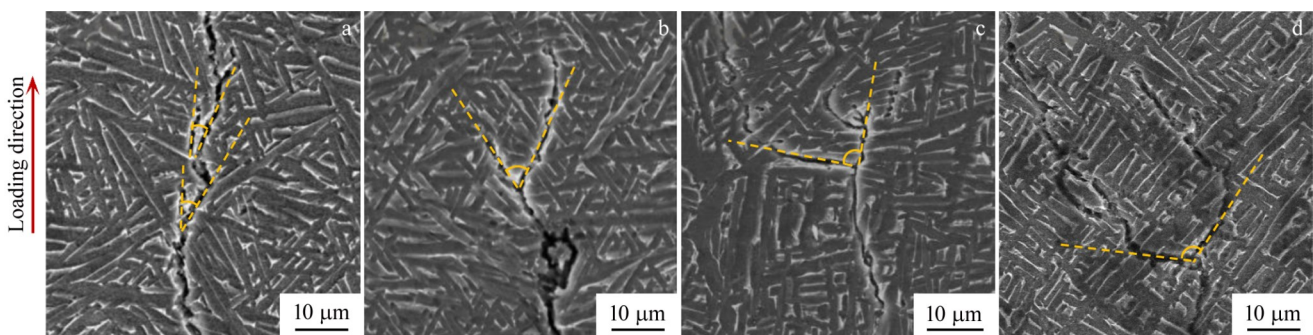


Fig. 15 Angles between main crack and secondary crack: (a)  $<30^\circ$ , (b) around  $60^\circ$ , (c) around  $90^\circ$ , and (d)  $>120^\circ$

thickness of specimen and thus present as equiaxed grains. The columnar  $\beta$  grains in ZD specimens are basically perpendicular to the crack plane and have angle of  $8^\circ$ – $15^\circ$  to the horizontal direction.

EBSD analysis was conducted to characterize the orientation of different directions, as shown in Fig. 17. The black part indicates the crack path. As shown in Fig. 17a, the multiple colors of  $\alpha$  laths imply different growing directions. It can be seen from pole figures in Fig. 17b that LMD Ti64 has a strong  $\langle 0001 \rangle$  texture in XD, YD and ZD. The maximum density values, i.e., mean uniform density (MUD), in XD, YD and ZD are 23.05, 36.66 and 32.36, respectively, indicating that  $\alpha$  phase  $\{0001\}$  family of crystal plane has obvious texture features.  $\beta$  phase also exhibits a strong  $\langle 001 \rangle$  crystal orientation, with the MUD value in ZD even reaching 47.15.

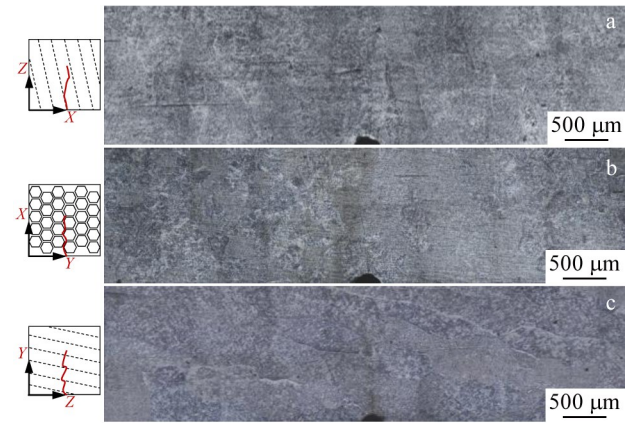


Fig.16 Microstructures of specimens in XD (a), YD (b), and ZD (c)

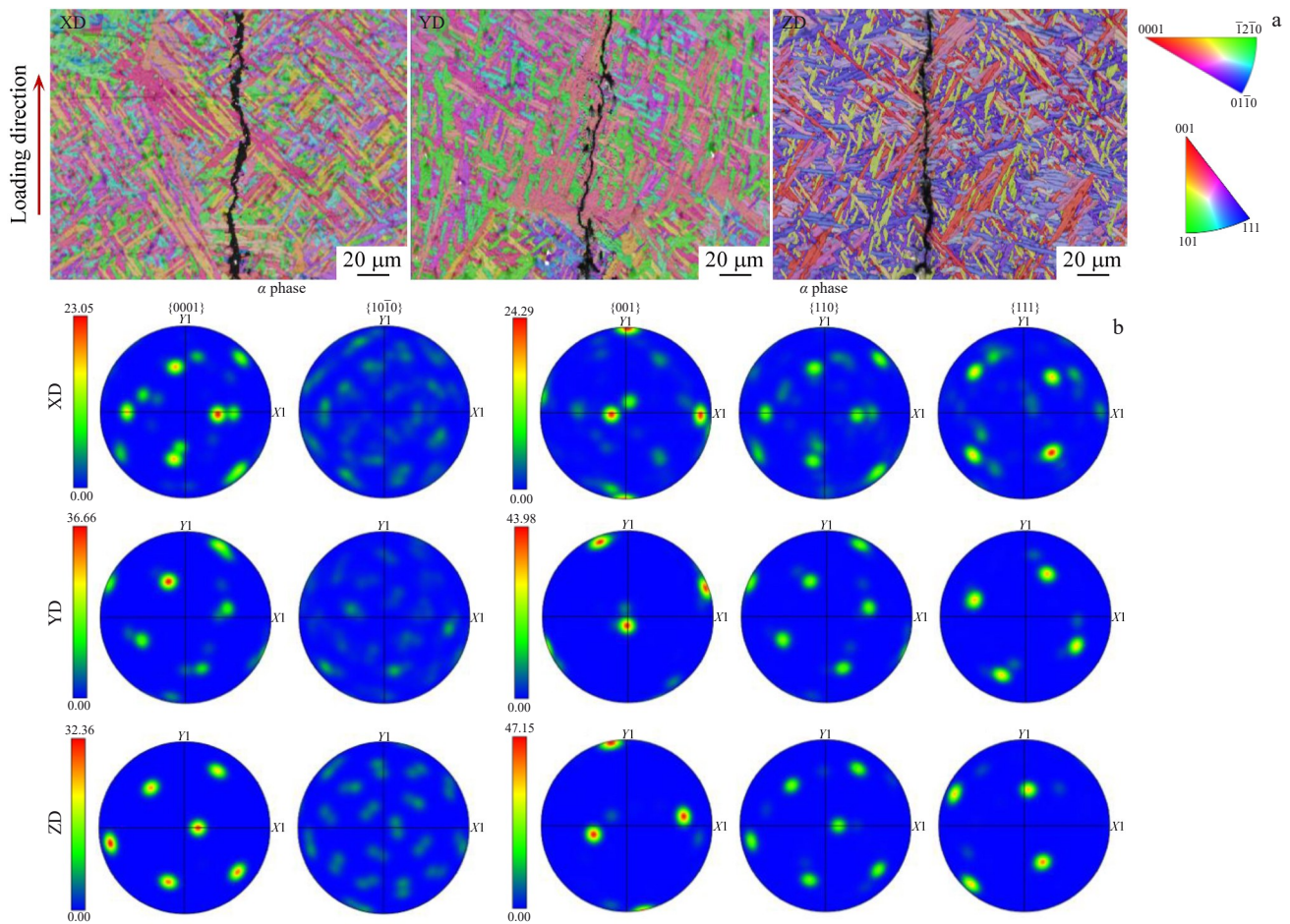


Fig.17 EBSD orientation maps of lateral surface of XD, YD, and ZD specimens (a) and corresponding pole figures (b)

In addition, the  $\langle 111 \rangle$  crystal orientation of  $\beta$  phase also has a weak texture. That is, the strong  $\langle 0001 \rangle // Z$  and  $\langle 001 \rangle // Z$  textures along the deposition direction are precisely the reason why the material still shows anisotropy in such short cracks.

### 3 Conclusions

1) The crack initiation of LMD Ti64 is affected by its microstructures. The fatigue crack initiation cycle number

follows a log-normal distribution. No significant difference is detected between XD and YD specimens. The resistance to crack initiation in ZD is slightly better than that in XD and YD, with a smaller dispersion. The crack initiation position angles are basically consistent with the normal distribution, while the crack initiation direction angles are mainly  $80^\circ$ – $100^\circ$ .

2) The velocity of early crack propagation is dominated by

the microstructures of LMD Ti64. Therein,  $\alpha$  colony, thick  $\alpha$  laths, basket weave and  $\alpha_{GB}$  may have a retarding effect on small crack propagation, while the  $\beta$  grain boundary and equiaxed  $\alpha$  may accelerate the fracture. LMD Ti64 has a typical small crack effect. The crack growth velocities in XD, YD and ZD are almost similar in the early stage, which are measured to be  $2 \times 10^{-8}$ – $3 \times 10^{-8}$  m/cycle.

3) The early crack propagation path is mainly affected by the  $\alpha$  laths and  $\alpha$  colony. Corresponding to  $(01\bar{1}0)$  prism slip,  $(0001)$  basal slip and  $(10\bar{1}0)$  prism slip, the crack tends to propagate along  $\alpha/\beta$  interfaces or directions perpendicular to  $\alpha/\beta$  interfaces. The crack is more likely to form a large deflection when passing through thick  $\alpha$  lath and basket weave structure. The deflection degree of the early crack propagation direction is correlated with the size of plastic zone.

4) The increased homogenization along principal slip system in hcp microstructure results in frequent occurrence of secondary cracks, which often have an angle of  $60^\circ$  to the main crack.

5) The LMD Ti64 has strong  $\langle 0001 \rangle // Z$  and  $\langle 001 \rangle // Z$  textures. Their crystallographic orientation will change as the direction of columnar  $\beta$  grains are turned over, resulting in anisotropy in crack initiation and early crack propagation of LMD Ti64.

## References

- Azarniya A, Colera X G, Mirzaali M J et al. *Journal of Alloys and Compounds*[J], 2019, 804: 163
- Ye H, Le F B, Wei C et al. *Journal of Alloys and Compounds*[J], 2021, 868: 159023
- Xiao Z X, Chen C P, Zhu H H et al. *Materials and Design*[J], 2020, 193: 108846
- Leuders S, Thöne M, Riemer A et al. *International Journal of Fatigue*[J], 2013, 48: 300
- Cain V, Thijs L, Van Humbeeck J et al. *Additive Manufacturing*[J], 2015, 5: 68
- Arola D, Williams C L. *International Journal of Fatigue*[J], 2002, 24(9): 923
- He Y, Huang W, Guo W G et al. *Materials*[J], 2023, 16(14): 5099
- Wu Z K, Wu S C, Bao J G et al. *International Journal of Fatigue*[J], 2021, 151: 106317
- Wu Z K, Wu S C, Qian W J et al. *Engineering Failure Analysis*[J], 2023, 149: 107265
- Wu H, Chi W Q, Xu W et al. *Engineering Fracture Mechanics*[J], 2022, 276: 108940
- Sun W B, Ma Y E, Huang W et al. *International Journal of Fatigue*[J], 2020, 130: 105260
- Walker K F, Liu Q C, Brandt M. *International Journal of Fatigue*[J], 2017, 104: 302
- Chastand V, Quaegebeur P, Maia W et al. *Materials Characterization*[J], 2018, 143: 76
- Gong H J, Rafi K, Gu H F et al. *Materials and Design*[J], 2015, 86: 545
- Chi W Q, Li G, Wang W J et al. *International Journal of Fatigue*[J], 2022, 160: 106862
- Li W Z, Qian F, Li J Y et al. *Additive Manufacturing*[J], 2023, 68: 103513
- Zheng Z P, Jin X, Bai Y C et al. *Materials Science and Engineering A*[J], 2022, 831: 142236
- Kasperovich G, Hausmann J. *Journal of Materials Processing Technology*[J], 2015, 220: 202
- Kelly S M, Kampe S L. *Metallurgical & Materials Transactions A*[J], 2004, 35(6): 1861
- Carroll B E, Palmer T A, Beese A M. *Acta Materialia*[J], 2015, 87: 309
- Syed A K, Ahmad B, Guo H et al. *Materials Science and Engineering*[J], 2019, 755: 246
- Kumar P, Ramamurty U. *Acta Materialia*[J], 2019, 169: 45
- Wu L L, Jiao Z H, Yu H C. *Fatigue and Fracture of Engineering Materials and Structures*[J], 2022, 45(8): 2174
- Pan X N, Hong Y S. *Fatigue and Fracture of Engineering Materials and Structures*[J], 2019, 42(9): 1950
- Zhu Y Y, Liu D, Tian X J et al. *Materials and Design*[J], 2014, 56: 445
- Haar G M T, Becker T H. *Materials*[J], 2018, 11(1): 146
- Wen X, Wan M P, Huang C W et al. *Materials Science and Engineering A*[J], 2019, 740: 121
- Shi X H, Zeng W D, Zhao Q Y. *Materials Science and Engineering A*[J], 2015, 636: 543
- Tan C S, Fan Y D, Sun Q Y et al. *Metals*[J], 2020, 10(8): 1058
- Mine Y, Takashima K, Bowen P. *Materials Science and Engineering A*[J], 2012, 532: 13
- Su H, Liu X, Sun C et al. *Fatigue and Fracture of Engineering Materials and Structures*[J], 2017, 40(6): 979
- Hong Y S, Sun C Q. *Theoretical and Applied Fracture Mechanics*[J], 2017, 92: 331
- Liu F L, Chen Y, Li L et al. *Journal of Materials Research and Technology*[J], 2022, 21: 2089
- Lu J X, Chang L, Wang J et al. *Materials Science and Engineering A*[J], 2018, 712: 199
- Xu Z W, Liu A, Wang X S et al. *International Journal of Fatigue*[J], 2020, 143: 106008
- Xu Z W, Liu A, Wang X S. *Materials Science and Engineering A*[J], 2019, 767: 138409
- Wu S C, Xiao T Q, Withers P J. *Engineering Fracture Mechanics*[J], 2017, 182: 127
- Sun C, Sun J, Chi W Q et al. *International Journal of Fatigue*[J], 2023, 176: 107897
- Chi W Q, Wang W J, Wu L et al. *International Journal of Fatigue*[J], 2023, 175: 107821
- Zhao S H, Yuan K B, Guo W G et al. *International Journal of Fatigue*[J], 2020, 136: 105629
- Zhai Y W, Lados D A, Brown E J et al. *International Journal of*

- Fatigue*[J], 2016, 93: 51
- 42 Peng C, Li P, Guo W et al. *3D Printing and Additive Manufacturing*[J], 2023, 10(1): 124
- 43 Lütjering G. *Materials Science and Engineering A*[J], 1998, 243(1-2): 32
- 44 Schroeder G, Albrecht J, Luetjering G. *Materials Science and Engineering A*[J], 2001, 319: 602
- 45 Suri S, Viswanathan G B, Neeraj T et al. *Acta Materialia*[J], 1999, 47: 1019
- 46 Li S K, Xiong B Q, Hui S X et al. *Materials Characterization*[J], 2008, 59(4): 397
- 47 Sansoz F, Ghonem H. *Materials Science and Engineering A*[J], 2003, 356(1-2): 81
- 48 Ravichandran K S. *Acta Metallurgica et Materialia*[J], 1991, 39: 401
- 49 Savage M F, Tatalovich J, Zupan M et al. *Materials Science and Engineering A*[J], 2001, 319: 398
- 50 Li G, Ke L, Ren X C et al. *International Journal of Fatigue*[J], 2023, 166: 107299
- 51 Tang D C, He X F, Wu B et al. *Theoretical and Applied Fracture Mechanics*[J], 2022, 119: 103322
- 52 Williams J C, Baggerly R G, Paton N E. *Metallurgical and Materials Transactions A*[J], 2002, 33: 837
- 53 Cleveringa H H M, Van der Giessen E, Needleman A. *Materials Science and Engineering A*[J], 2001, 317(1-2): 37
- 54 Wang F, Lei L, Fu X et al. *Journal of Materials Science and Technology*[J], 2023, 132: 166
- 55 Zhang Y L, Chen Z, Qu S J et al. *Journal of Materials Science and Technology*[J], 2021, 70: 113

## 激光金属沉积 Ti-6Al-4V 钛合金在高周疲劳加载下的早期裂纹扩展行为

李艳萍<sup>1</sup>, 黄 玮<sup>1</sup>, 赫 燕<sup>1</sup>, 徐 丰<sup>2</sup>, 赵思晗<sup>1</sup>, 郭伟国<sup>1</sup>

(1. 西北工业大学 航空学院, 陕西 西安 710072)

(2. 西北工业大学 航天学院, 陕西 西安 710072)

**摘 要:** 裂纹的萌生和早期扩展对材料的整体疲劳寿命具有重要意义。为了了解激光金属沉积钛合金 (LMD Ti64) 在断裂早期的各向异性断裂行为, 对 3 个不同方向的试样以及锻造试样进行了 4 点弯曲疲劳试验。结果表明, LMD Ti64 具有各向异性的裂纹萌生和早期扩展行为: 在垂直于沉积方向上, 表现出比其余两个方向更好的疲劳抗性; 裂纹的萌生位置和早期的扩展路径主要由 U 型缺口附近的微观结构主导; LMD Ti64 具有典型的小裂纹效应, 3 个方向的早期裂纹扩展速度相似; 受滑移系统的影响, LMD Ti64 的扩展路径上频繁出现二次裂纹, 这些二次裂纹通常与主裂纹呈 60° 角。通过电子背散射衍射分析表明, LMD Ti64 具有择优取向, 表现为强  $\langle 0001 \rangle // Z$  织构和  $\langle 001 \rangle // Z$  织构。当  $\beta$  柱状晶粒的方向发生翻转时, 其晶体学取向也会随之改变, 从而导致 LMD Ti64 在裂纹萌生和早期裂纹扩展过程中出现疲劳各向异性。

**关键词:** 疲劳抗性; 裂纹扩展行为; 微观结构; 激光金属沉积; Ti-6Al-4V; 各向异性

作者简介: 李艳萍, 女, 1988 年生, 博士生, 西北工业大学航空学院, 陕西 西安 710072, E-mail: yanping.li@mail.nwpu.edu.cn